

1 **Multispectral Fundus Photography of Choroidal Nevi with Trans-Palpebral**

2 **Illumination**

3 Mojtaba Rahimi¹, Alfa Rossi¹, Taeyoon Son¹, Albert K. Dadzie¹, Behrouz Ebrahimi¹, Mansour

4 Abtahi¹, Michael J. Heiferman², and Xincheng Yao^{1,2}

5 ¹Department of Biomedical Engineering, University of Illinois Chicago, Chicago, IL 60607,

6 USA; ²Department of Ophthalmology and Visual Sciences, University of Illinois Chicago,

7 Chicago, IL, 60612, USA

8 **Corresponding author:**

9 Xincheng Yao, PhD

10 Richard & Loan Hill Chair Professor

11 Department of Biomedical Engineering (MC 563)

12 University of Illinois Chicago

13 Clinical Sciences North, Suite W103, Room 164D

14 820 South Wood Street, Chicago, IL 60612

15 Tel: (312)413-2016; Fax: (312)996-4644; Email: xcy@uic.edu

16 **Word Count:** 4145

17 **Funding/Support:** National Eye Institute (R01 EY023522, R01 EY029673, R01 EY030101,

18 R01 EY030842, P30EY001792); Research to Prevent Blindness; Richard and Loan Hill

19 Endowment.

20 **Commercial Relationships:** None

21 **Abstract**

22 **Purpose:** To investigate the spectral characteristics of choroidal nevi and assess the
23 feasibility of quantifying the basal diameter of choroidal nevi using multispectral fundus
24 images captured with trans-palpebral illumination.

25 **Methods:** The study employed a widefield fundus camera with multispectral (625 nm, 780
26 nm, 850 nm, and 970 nm) trans-palpebral illumination. Geometric features of choroidal nevi,
27 including border clarity, overlying drusen, and lesion basal diameter, were characterized.
28 Clinical imagers, including scanning laser ophthalmoscopy (SLO), autofluorescence (AF),
29 and optical coherence tomography (OCT), were utilized for comparative assessment.

30 **Results:** Fundus images captured with trans-palpebral illumination depicted nevi as dark
31 regions with high contrast against the background. Near-infrared (NIR) fundus images
32 provided enhanced visibility of lesion borders compared to visible light fundus images and
33 SLO images. Lesion-background contrast measurements revealed 635 nm SLO at 11% and
34 625 nm fundus at 42%. Significantly enhanced contrasts were observed in NIR fundus
35 images at 780 nm (73%), 850 nm (63%), and 970 nm (67%). For quantifying the basal
36 diameter of nevi, NIR fundus images at 780 nm and 850 nm yielded a deviation of less than
37 10% when compared to OCT B-scan measurements.

38 **Conclusion:** NIR fundus photography with trans-palpebral illumination enhances nevi
39 visibility and boundary definition compared to SLO. Agreement in basal diameter
40 measurements with OCT validates the accuracy and reliability of this method for choroidal
41 nevi assessment.

42 **Translational Relevance:** Multispectral fundus imaging with trans-palpebral illumination
43 improves choroidal nevi visibility, accurately measures basal diameter, promising to enhance
44 clinical practices in screening, diagnosis, and monitoring of choroidal nevi.

45 **Introduction**

46 Choroidal nevus is the most frequently occurring primary intraocular tumor¹. This condition
47 poses two associated risks: firstly, a benign nevus can transform into malignant melanoma,
48 with risks of melanoma-related metastasis and mortality; and secondly, nevi may lead to
49 vision impairment from subretinal fluid or secondary choroidal neovascularization^{2,3}. Early
50 detection and careful progression monitoring of choroidal nevi are crucial as they are early-
51 stage precursors to choroidal melanomas⁴. Shields et al.⁵ have proposed several risk factors
52 associated with the transformation of choroidal nevus into melanoma. These factors include
53 lesion thickness, the presence of subretinal fluid, visual symptoms, the presence of orange
54 pigment, and ultrasound acoustic hollowness. Clinicians rely on various imaging modalities,
55 including color fundus photography (CFP)⁶, scanning laser ophthalmoscopy (SLO)⁷, fundus
56 autofluorescence (AF)⁸, optical coherence tomography (OCT)^{9,10}, and ultrasonography¹¹, to
57 assess these risk factors. Each of these imaging modalities has its own strengths and
58 limitations. Consequently, multimodal imaging is often employed for the assessment of
59 choroidal nevi⁵. CFP and SLO provide two-dimensional lateral profiles of the lesion. In
60 contrast, OCT and ultrasound images reveal depth information of nevi. Additionally, AF
61 image can reveal the accumulation of lipofuscin, seen clinically as overlying orange pigment,
62 suggestive of tumor activity. Ultrasonography is currently the gold standard for the
63 measurement of intraocular tumors and provides an accurate measurement of tumor
64 thickness using A-scan. However, it is acknowledged that B-scan ultrasonography
65 measurements of lateral diameter are less precise for choroidal tumors, especially for
66 choroidal nevi that appear flat due to their thinness⁷. Nevertheless, small choroidal tumors
67 that might escape detection via ultrasonography can be objectively measured using OCT
68 which provides high-resolution cross sectional imaging of choroidal lesions^{10,12}. However,
69 OCT is still relatively expensive, requires pharmacologic dilation, and can be inaccessible for
70 patients in rural and underserved areas where advanced imaging equipment and skilled
71 operators are limited.

72 Conventional CFP is employed for imaging choroidal lesions due to its availability and cost-
73 efficiency. However, it presents two significant limitations for the imaging and assessment of
74 choroidal nevi: a limited field of view (FOV) and low choroidal lesion contrast. FOV of
75 traditional fundus cameras typically ranges from 30° to 45° visual angle (45° to 68° eye
76 angle) as it requires careful allocation of the available pupil for both illuminating and imaging
77 paths^{13, 14}. Consequently, it becomes challenging to detect choroidal nevi, especially those
78 located in the periphery of the fundus. Ultra-widefield SLO imaging systems (e.g., Optos),
79 offering a 134° visual angle (200° eye angle) FOV¹⁵, serve as an alternative means to image
80 choroidal nevi and measure tumor basal diameter⁷. However, SLO imagers incorporate
81 several laser sources and scanning systems that increase the cost and complexity of the
82 system.

83 Trans-palpebral illumination has been investigated as an alternative illumination method in
84 fundus photography, enabling widefield fundus imaging without the need for pupil dilation¹⁶⁻
85 ¹⁸. Son et al¹⁷. achieved a 93° visual angle (140° eye angle) FOV in a single snapshot fundus
86 image utilizing trans-palpebral illumination. The incorporation of narrow-band light emitting
87 diodes (LEDs) into this method has demonstrated the capability to enable multispectral
88 imaging of the retina and choroid¹⁷. In contrast to traditional fundus photography which relies
89 on white light illumination to capture a color fundus image by combining reflection
90 information from several retinal layers^{19, 20}, multispectral fundus photography selectively
91 image different layers of retina and choroid²¹. Generally, longer wavelengths of light allow
92 deeper penetration through the retina into the choroid (Figure 1 (B)). Therefore, short visible
93 light predominantly uncovers superficial retinal structure, while long visible wavelength and
94 near-infrared (NIR) light images are attributed to both the retinal and choroidal layers²².
95 Choroidal nevi originate within the choroid beneath the retina and can impact the overlying
96 retinal pigment epithelium (RPE), resulting in features like atrophy, drusen, and lipofuscin
97 accumulation²³. As a result, multispectral fundus photography using long visible and NIR
98 wavelengths promises a practical solution for selectively capturing these choroidal lesions.

99 However, most multispectral fundus devices are essentially conventional fundus cameras
100 that incorporate multiple light sources or tunable filters into their trans-pupillary illumination²⁴⁻
101 ²⁶. Consequently, they tend to have bulky dimensions, and spatial scanning is required due
102 to the limited FOV.

103 Previous studies by Muftuoglu et al.⁶ and Venkatesh, et al²⁷. have compared the
104 effectiveness of multispectral SLO imaging to CFP in identifying choroidal lesions. They
105 reported that multispectral SLO provides similar information with CFP for the features of
106 choroidal lesions. Moreover, Azzolini et al.²⁸ demonstrated that the retro-mode and dark-field
107 mode of SLO can enhance the contrast of choroidal nevi and delineate lesion margins in NIR
108 wavelength. However, this enhancement necessitates specific adjustments to the confocal
109 laser scanning system. On the other hand, trans-palpebral illumination naturally fulfills the
110 requirement for a dark-field imaging condition, enhancing the contrast of choroidal lesions. In
111 this oblique illumination method, light is delivered from a region outside of the pupil, typically
112 with a ~4 mm distance from the limbus. This contrast enhancement is valuable for detecting
113 and monitoring the basal diameter of choroidal nevi. Furthermore, the cost-effectiveness of
114 multispectral fundus photography with trans-palpebral illumination, along with the absence of
115 the need for pupillary dilation, indicates its potential as an optimal choice for screening the
116 general population for choroidal nevi. Choroidal nevi affect approximately 5% of the
117 population and are recommended to be monitored at least once per year, given that roughly
118 one-third of uveal melanomas are asymptomatic^{3,29}. Therefore, this method can empower
119 referring healthcare professionals, such as primary care physicians and optometrists, to
120 screen and triage patients more effectively based on geometric features of the lesion. This
121 study aims to investigate the effectiveness of multispectral fundus photography with trans-
122 palpebral illumination as an affordable approach for high contrast imaging and quantitative
123 assessment of choroidal nevi.

124 **Methods**

125 ***Experimental setup***

126 Figure 1 (A) illustrates the optical configuration of the widefield fundus camera system,
127 including trans-palpebral illumination for multispectral fundus images. The first lens group
128 (L1, L2, and L3) consists of a meniscus lens (L1: LE1234-A, Thorlabs Inc., Newton, NJ), a
129 plano-convex lens (L2: 67–152, Edmund Optics Inc., Barrington, NJ), and a double-convex
130 lens (L3: 63–688, Edmund Optics Inc., Barrington, NJ, USA). This lens assembly collects
131 light from the pupil and generates an aerial image in front of the relay optics. Subsequently,
132 a triplet achromatic lens (L4: 67–422, Edmund Optics Inc., Barrington, NJ, USA) and the
133 camera lens (33–303, Edmund Optics Inc., Barrington, NJ, USA) are precisely positioned to
134 relay this aerial image onto the camera sensor. The removal of the infrared filter from the
135 color CMOS camera (DFK 37BUX250, The Imaging Source Europe GmbH, Bremen,
136 Germany) enables the detection of NIR light. By delivering light through the eyelid, the trans-
137 palpebral illuminator provides a convenient means of illuminating the interior of the eye. It
138 comprises 1-to-4 fan-out fiber bundles (BF46LS01, Thorlabs Inc., Newton, NJ). Each
139 individual optical fiber within these bundles possesses a diameter of 600 μm and a
140 numerical aperture of 0.39. These optical fibers are connected to narrow-band LED light
141 sources with center wavelengths of 625 nm (M625L4, Thorlabs Inc., Newton, NJ), 780 nm
142 (M780L3, Thorlabs Inc., Newton, NJ), 850 nm (M850LP1, Thorlabs Inc., Newton, NJ), and
143 970 nm (M970L4, Thorlabs Inc., Newton, NJ). The optical spectrum of the light sources is
144 shown in Figure 1 (C). The specifics of the optical system design have been elaborated upon
145 in previous publication¹⁷.

146 ***Human subjects and imaging procedures***

147 This study received approval from the Institutional Review Board at the University of Illinois
148 Chicago and adhered to the ethical principles outlined in the Declaration of Helsinki. It
149 included eight eyes from eight patients previously diagnosed with a choroidal nevus.
150 Informed consent was obtained from each subject prior to imaging. All participants
151 underwent comprehensive clinical multimodal imaging procedures, which included ultra-
152 widefield SLO, fundus AF, NIR reflectance, and spectral domain OCT enabling a

153 comparative analysis. OCT and NIR reflectance were performed using Spectralis
154 (Heidelberg Engineering GmbH; Heidelberg, Germany). SLO and AF images were captured
155 using Optos California (Optos; Marlborough, MA, USA). Furthermore, multispectral fundus
156 images were obtained using the fundus camera equipped with trans-palpebral illumination.
157 For image stability, participants were positioned with their foreheads and chins resting on
158 supports. The trans-palpebral illuminator was gently positioned on the eyelid and individually
159 adjusted based on the live preview image. A custom LabVIEW interface was used to enable
160 real-time monitoring, facilitating the alignment of the fundus camera and trans-palpebral
161 illuminator, as well as the sequential capture of fundus images. To aid in maintaining fixation
162 during the imaging procedure, a low-intensity LED served as a visual target.

163 ***Light safety***

164 The ISO standard for "Ophthalmic Instrument- Fundus camera"³⁰ is employed to evaluate
165 ocular light safety for multispectral fundus imaging with trans-palpebral illumination,
166 considering both photochemical and thermal hazards. The LED powers at the output of the
167 fiber were adjusted to 15 mW, 10 mW, 7 mW, and 5 mW for 625 nm, 780 nm, 850 nm, and
168 970 nm illuminations, respectively. According to the ISO standard, to prevent thermal
169 hazards, the highest allowable weighted power intensity on the retina is 700 mW/cm². The
170 methodology for calculating the illuminated retinal area during trans-palpebral illumination
171 was explained in a previous publication³¹. Following the assessment of thermal hazards, the
172 calculated equivalent power levels for the light sources at 625 nm, 780 nm, 850 nm, and 970
173 nm were determined to be 13.1 mW/cm², 15.9 mW/cm², 14.4 mW/cm², and 7.9 mW/cm²,
174 respectively. The calculated weighted power intensity for all of these wavelengths was found
175 to be significantly lower than the established allowable limit, indicating that there were no
176 thermal hazard concerns associated with any of the considered wavelengths. The
177 photochemical hazard is negligible for NIR wavelengths. The weighted irradiance for the
178 visible light was computed utilizing the photochemical hazard weighing function specified in
179 the ISO standard. For 625 nm illumination, the aphakic photochemical hazard weighing

180 function is determined to be 0.001. Consequently, the calculated maximum permissible
181 exposure time exceeds 24 hours. A comprehensive description of the ocular safety
182 calculations can be found in a prior publication³².

183 **Results**

184 ***Lateral Characterization***

185 Figure 2 represents the results of imaging a participant diagnosed with a choroidal nevus. In
186 Figure 2 (A1) and (A2), the SLO image and an enlarged view of the nevus region are
187 presented, respectively. Figure 2 (B1) to (B4) shows the green and red channels of the SLO
188 image, the AF image, and the NIR reflectance images. Representative multispectral fundus
189 images with 625 nm, 780 nm, 850 nm, and 970 nm trans-palpebral illumination are shown in
190 Figure 2 (C1) to Figure 2 (C4), respectively. For direct comparison, the green and red
191 channels of the SLO image and AF image have been cropped to correspond to the same
192 region depicted in the fundus images. The green channel of SLO (Figure 2 (B1)), generated
193 through a 532 nm laser, provides insight into the superficial structures of the retina to the
194 RPE layer. In contrast, the red channel (Figure 2 (B2)), produced with a 635 nm laser,
195 predominantly accentuates the deeper retinal structures, encompassing the RPE through the
196 choroid. The AF image (Figure 2 (B3)) reveals the minimal fluorescent properties at the RPE
197 layer. An 815 nm laser is used to capture the NIR reflectance image (Figure 2 (B4)). The
198 fundus image captured using visible light (Figure 2 (C1)) reveals retinal veins and some
199 choroidal structure due to the partial penetration of red light through the RPE layer. When
200 employing 780 nm illumination (Figure 2 (C2)), an improved depiction of the choroidal
201 vasculature is achieved compared to red illumination. This aligns with the concept of
202 reduced melanin absorption in the RPE, consequently allowing enhanced NIR light
203 penetration to reveal the choroidal vasculature. By extending the illumination wavelength to
204 970 nm (Figure 2 (C4)), predominantly choroidal veins became discernible in the fundus
205 image.

206 To facilitate a more straightforward comparison of nevi using various imaging modalities,
207 Figure 2 (D) presents the enlarged nevus region within the multispectral fundus images
208 captured under trans-palpebral illumination. Additionally, Figure 2 (E) displays the enlarged
209 nevus region within the green and red channels of the SLO (Figure 2 (E1 and E2)), AF
210 (Figure 2 (E3)), and NIR (Figure 2 (E4)) images. The nevus is observed as a distinct dark
211 region in both the red (Figure 2 (D1)) and NIR (Figure 2 (D2-D4)) fundus images,
212 significantly more visible in comparison to the SLO image (Figure 2 (E2)) and the AF image
213 (Figure 2 (E3)). Additionally, the NIR fundus images exhibited an improved capacity to
214 illustrate clear boundaries of the nevus, as well as to highlight information about overlying
215 drusen. Analysis of the green and red channels of the SLO image indicates that the green
216 channel (Figure 2 (E1)) does not reveal the nevus, while the nevus appears as a hypo-
217 reflective region in the red channel (Figure 2 (E2)), though its boundaries remain unclear.
218 Furthermore, the nevus does not exhibit significant autofluorescence features in the AF
219 image ((Figure 2 (E3))) due to absence of overlying orange pigment. However, the overlying
220 drusen can be seen faintly in the AF image. In the NIR reflectance image (Figure 2 (E4)), the
221 nevus is characterized by an iso-reflective region with overlying drusen. The diameter of the
222 nevus is measured utilizing the measurement tool in the Optos-Advance software (Figure 2
223 (A2)). The diameter measurements in the SLO image rely on the color contrast of the lesion
224 within the image, a method described by Pe'er et al⁷.

225 To evaluate the measurement of choroidal nevus basal diameter in fundus images, the
226 intensity line profiles derived from fundus images captured under visible and NIR illumination
227 are analyzed. The intensity line profile of the lesion, indicated by a dashed line in Figure 2
228 (D1), is presented in Figure 3 (A). The full width at half maximum (FWHM) of the normalized
229 intensity profile serves as the reference for measurement of nevus basal diameter in fundus
230 images. Furthermore, Figure 3 (B) displays the intensity profile of the same region in the
231 green and red channels of SLO, AF, and NIR reflectance images, showing the presence of
232 overlying drusen in all intensity profiles. Analyzing the intensity profile of the nevus in the

233 green and red channels of SLO reveals that the contrast of the lesion compared to the
234 surrounding region originates from the red channel. This contrast is somewhat less
235 pronounced than the contrast observed in the fundus images. Lesion-background mean
236 contrast was considered to quantify the visibility of the nevus in the images. The
237 straightforward definition of Lesion-background contrast (C) is as follows:³³

$$238 \quad C = \frac{|\bar{I}_b - \bar{I}_l|}{\bar{I}_b + \bar{I}_l} \quad (1)$$

239 where \bar{I}_l and \bar{I}_b are the mean intensity of the lesion and its background, respectively. The red
240 channel of the SLO image and the 625 nm fundus image exhibited lesion-background
241 contrasts of 11% and 42%, respectively. However, fundus images with NIR illumination at
242 780 nm, 850 nm, and 970 nm showed higher lesion-background contrasts, measuring 73%,
243 63%, and 67%, respectively. The results of nevus basal diameter measurement and
244 quantification of lesion-background contrasts for the other seven subjects are summarized in
245 Table 1. The consistency of the results across all subjects supports the validity of the study.

246 ***Axial Characterization***

247 To characterize the axial property of the choroidal nevus, the OCT B-scan of the nevus
248 region is analyzed. Figure 4 (B) presents the OCT B-scan images of the nevus which
249 exhibits hyperreflectivity along the anterior surface of the lesion, accompanied by dark
250 posterior shadowing. The discernible pattern observed in the choroidal layers of the OCT B-
251 scan greatly aids in measuring the basal diameter of the nevus. To assess the accuracy of
252 quantifying the basal diameter of the nevus in fundus images, the nevus basal diameter was
253 measured using the measurement tool in the Heidelberg Spectralis system within the OCT
254 B-scan (Figure 4 (B)). The dark posterior shadowing observed in the nevus was utilized to
255 define boundaries for diameter measurements in the OCT B-scan, as previously described
256 by Jonna et al⁹. In Table 1, the results of basal diameter measurements in fundus images
257 are compared with those obtained in the OCT B-scan, used as a reference. The results
258 show a deviation of less than 10% in the NIR fundus images at 780 nm and 850 nm

259 compared with measurements obtained from the OCT B-scan, verifying the feasibility and
260 accuracy of quantifying choroidal nevus basal diameter in fundus images. The slight
261 variations in values observed for different wavelengths can be attributed to differences in the
262 nevus shape at various depths and focal planes corresponding to these wavelengths. By
263 increasing the wavelength to 970 nm, the heightened transparency results in reduced
264 contrast and decreased accuracy in measuring lesion diameter. For the third subject listed in
265 Table 1, the 625 nm fundus image exhibited reflection artifacts in the lesion region, rendering
266 the measurements inaccurate. Consequently, this data was excluded from the results.

267 In contrast to the cross-sectional B-scan image, the en face OCT image offers a view that
268 resembles traditional 2D imaging. To compare the appearance of the nevus in fundus and
269 OCT en face images, averaged en face OCT images were generated after flattening and
270 registering the OCT B-scans of the nevus region (Figure 4 (C)). In OCT en face images that
271 average retinal layers above the RPE layer (Figure 4 (C1)), the retinal vasculature becomes
272 visible, similar to the green channel of the SLO image (Figure 2 (E1)). In the en face image
273 comprising the RPE layer (Figure 4 (C2)) presence of overlying drusen and RPE alterations
274 can be identified. Additionally, Figure 4 (C3) and Figure 4 (C4) depict the choriocapillaris and
275 medium choroidal vessels of Sattler's layer, respectively, which exhibit a similar structure to
276 the fundus images captured using 625 nm and 780 nm trans-palpebral illumination (as seen
277 in Figure 2 (D1 and D2)). In Figure 4 (C5), large choroidal vessels in Haller's layer are
278 visible, and Figure 4 (C6) showcases signals originating from the deep choroid and sclera.
279 These findings correlate with the fundus images captured at longer wavelengths of 850 nm
280 and 970 nm (as shown in Figure 2 (D3 and D4)). The nevus appears as a dark region in
281 OCT en face images from the choroidal layers, resembling the appearance in the fundus
282 image with NIR trans-palpebral illumination. However, the fundus images display overlying
283 drusen, attributable to the fact that longer wavelengths, penetrating deeper layers, still carry
284 information from the layers above.

285 **Discussion**

286 The spectral characteristics of choroidal nevi and the feasibility of quantifying the basal
287 diameter of these nevi using multispectral fundus images captured with trans-palpebral
288 illumination was investigated. Fundus images captured with the NIR wavelength range
289 revealed choroidal nevi as distinct dark regions with significantly enhanced contrast against
290 the surrounding fundus tissue. The clearer delineation of the nevus boundaries allows
291 clinicians to detect and precisely assess the location and extent of the lesion. Validation of
292 the feasibility of quantifying choroidal nevus diameter in fundus images is achieved by
293 measuring nevus basal diameter in NIR images and comparing it with reference
294 measurements obtained from OCT B-scans.

295 Previous studies have highlighted the effectiveness of multispectral fundus imaging in
296 selectively capturing detailed images of the retina and choroid³⁴. It is widely recognized that
297 choroidal structures can be effectively visualized through the utilization of NIR illumination.
298 According to the study conducted by Burgos-Fernández et al.²⁶, choroidal nevi show low
299 reflectance and good contrast at NIR wavelengths in multispectral fundus images. However,
300 their fundus camera utilized trans-pupillary illumination, which restricted the system's FOV to
301 30° visual angle (45° eye angle). In addition, Muftuoglu et al.⁶ have compared the
302 multispectral SLO system with CFP. Their multispectral SLO system provided pseudo-color
303 image using three different wavelengths including blue (486 nm), green (518 nm) and NIR
304 (815 nm). Their findings indicated that the multispectral SLO system could offer similar
305 insights to CFP regarding the characteristics of choroidal lesions, including border
306 delineation and the detection of overlying drusen. However, the NIR channel of the
307 multispectral SLO system underestimated the extent of choroidal lesions by approximately
308 33%. This discrepancy in delineating lesion borders when compared to CFP could be
309 attributed to the confocal imaging system of SLO, which possesses a limited depth of field, in
310 contrast to CFP's ability to combine reflection data from various depths within the fundus.
311 Furthermore, Azzolini et al.²⁸ have shown that utilizing annular and deviated apertures in the

312 confocal plane of SLO provides dark-field and retro-mode imaging condition in SLO system,
313 which enhanced the contrast of choroidal nevi in NIR SLO image.

314 In contrast to the SLO system that relies on multiple lasers and mechanical scanning
315 mechanisms, the presented multispectral fundus camera employs LEDs which not only
316 significantly reduce costs but also results in a portable device. These advantages are
317 particularly beneficial for facilitating the emerging field of telemedicine, especially in rural or
318 underserved areas. The fundus camera with trans-palpebral illumination can capture a
319 snapshot with a FOV up to 93° visual angle (140° eye angle) without the need for pupil
320 dilation. By utilizing a fixation target, this FOV can be further expanded to 134° visual angle
321 (200° eye angle)¹⁷. Furthermore, trans-palpebral illumination benefits from a dark-field
322 imaging condition. This condition is achieved by completely separating the illumination and
323 imaging paths, preventing any specular reflectance light from reaching the camera. The
324 contrast of choroidal nevi within fundus images is primarily a result of heightened light
325 absorption by the melanin and melanocytes present in the nevi³⁴. Melanin absorption
326 decreases with increasing wavelength. Consequently, NIR wavelengths can penetrate
327 deeply into the normal choroid and are backscattered from the sclera. The absence of
328 specular reflection from the surface of the nevus in the dark-field imaging condition, along
329 with the backscattered light from the normal choroid tissue, leads to high-contrast in the NIR
330 fundus images with trans-palpebral illumination.

331 The practical application of trans-palpebral illumination for visible light fundus imaging poses
332 challenges due to the efficiency of light transmission through the eyelid and sclera. It has
333 been demonstrated that this efficiency depends on several factors, including the wavelength
334 of illumination, the location of illuminator, and the complexion of the subject¹⁷. However, the
335 efficiency of NIR wavelengths in trans-palpebral illumination is significantly higher, by
336 multiple orders of magnitude, compared to visible wavelengths¹⁷. Consequently, there are no
337 limitations regarding the efficiency of NIR wavelengths for imaging choroidal nevi. Moreover,
338 cutaneous pigmentation effect can be easily compensated for by adjusting the power of the

339 light source, without concerns about light safety. Additionally, an analysis of the spatial
340 dependence of spectral efficiency has shown that the location of illumination significantly
341 affects the efficiency of visible light, while NIR light demonstrates no significant location
342 dependency³¹. These findings along with the affordability and the absence of the need for
343 pupil dilation strongly support the notion that fundus imaging with NIR trans-palpebral
344 illumination offers a straightforward and practical approach for detection and screening of
345 choroidal nevi in the general population. This method has the potential to enable healthcare
346 professionals to assess choroidal nevi more effectively and to expedite referrals to ocular
347 oncologists, ensuring that patients receive timely and appropriate care.

348 **Conclusion**

349 In conclusion, this study highlights the significant advantages of fundus imaging with NIR
350 trans-palpebral illumination for detecting and assessing choroidal nevi. This approach
351 enhances nevus visibility and boundary definition compared to SLO. The close agreement
352 between nevus basal diameter measurements in NIR fundus images and OCT B-scans
353 confirms the accuracy and reliability of this technique for measurement of choroidal nevi.
354 This method shows promise in enhancing clinical practice, improving the screening,
355 diagnosis, and monitoring of choroidal nevi.

356 Reference

- 357 1. Shields JA, Shields CL. *Intraocular tumors: an atlas and textbook*: Lippincott Williams &
358 Wilkins; 2008.
- 359 2. Shields CL, Lally SE, Dalvin LA, et al. White paper on ophthalmic imaging for choroidal nevus
360 identification and transformation into melanoma. *Translational Vision Science & Technology*
361 2021;10:24-24.
- 362 3. Qiu M, Shields CL. Choroidal nevus in the United States adult population: racial disparities
363 and associated factors in the National Health and Nutrition Examination Survey. *Ophthalmology*
364 2015;122:2071-2083.
- 365 4. Geiger F, Said S, Bajka A, et al. Assessing Choroidal Nevi, Melanomas and Indeterminate
366 Melanocytic Lesions Using Multimodal Imaging—A Retrospective Chart Review. *Current Oncology*
367 2022;29:1018-1028.
- 368 5. Shields CL, Dalvin LA, Ancona-Lezama D, et al. Choroidal nevus imaging features in 3,806
369 cases and risk factors for transformation into melanoma in 2,355 cases: the 2020 Taylor R. Smith and
370 Victor T. Curtin Lecture. *Retina* 2019;39:1840-1851.
- 371 6. Muftuoglu IK, Gaber R, Bartsch D-U, Meshi A, Goldbaum M, Freeman WR. Comparison of
372 conventional color fundus photography and multicolor imaging in choroidal or retinal lesions.
373 *Graefes Archive for Clinical and Experimental Ophthalmology* 2018;256:643-649.
- 374 7. Pe'er J, Sancho C, Cantu J, et al. Measurement of choroidal melanoma basal diameter by
375 wide-angle digital fundus camera: a comparison with ultrasound measurement. *Ophthalmologica*
376 2006;220:194-197.
- 377 8. Vallabh N, Sahni J, Parkes C, Czanner G, Heimann H, Damato B. Near-infrared reflectance and
378 autofluorescence imaging characteristics of choroidal nevi. *Eye* 2016;30:1593-1597.
- 379 9. Jonna G, Daniels AB. Enhanced depth imaging OCT of ultrasonographically flat choroidal nevi
380 demonstrates 5 distinct patterns. *Ophthalmology Retina* 2019;3:270-277.
- 381 10. Torres VL, Brugnoli N, Kaiser PK, Singh AD. Optical coherence tomography enhanced depth
382 imaging of choroidal tumors. *American journal of ophthalmology* 2011;151:586-593. e582.
- 383 11. Daniels AB, Veverka KK, Patel SN, Sculley L, Munn G, Pulido JS. Computing uveal melanoma
384 basal diameters: a comparative analysis of several novel techniques with improved accuracy.
385 *International Journal of Retina and Vitreous* 2019;5:1-10.
- 386 12. Shields CL, Kaliki S, Rojanaporn D, Ferenczy SR, Shields JA. Enhanced depth imaging optical
387 coherence tomography of small choroidal melanoma: comparison with choroidal nevus. *Archives of*
388 *Ophthalmology* 2012;130:850-856.
- 389 13. Yao X, Son T, Ma J. Developing portable widefield fundus camera for teleophthalmology:
390 Technical challenges and potential solutions. *Experimental Biology and Medicine* 2022;247:289-299.
- 391 14. Rossi A, Rahimi M, Le D, et al. Portable widefield fundus camera with high dynamic range
392 imaging capability. *Biomedical Optics Express* 2023;14:906-917.
- 393 15. Patel SN, Shi A, Wibbelsman TD, Klufas MA. Ultra-widefield retinal imaging: an update on
394 recent advances. *Therapeutic advances in ophthalmology* 2020;12:2515841419899495.
- 395 16. Toslak D, Thapa D, Chen Y, Erol MK, Chan RP, Yao X. Trans-palpebral illumination: an
396 approach for wide-angle fundus photography without the need for pupil dilation. *Optics letters*
397 2016;41:2688.
- 398 17. Son T, Ma J, Toslak D, et al. Light color efficiency-balanced trans-palpebral illumination for
399 widefield fundus photography of the retina and choroid. *Scientific Reports* 2022;12:13850.
- 400 18. Rahimi M, Rossi A, Son T, Yao X. High dynamic range fundus camera with trans-palpebral
401 illumination. *Investigative Ophthalmology & Visual Science* 2023;64:5016-5016.
- 402 19. Panwar N, Huang P, Lee J, et al. Fundus photography in the 21st century—a review of recent
403 technological advances and their implications for worldwide healthcare. *Telemedicine and e-Health*
404 2016;22:198-208.

- 405 20. Rossi A, Rahimi M, Son T, Chan RP, Heiferman MJ, Yao X. Preserving polarization maintaining
406 photons for enhanced contrast imaging of the retina. *Biomedical Optics Express* 2023;14:5932-5945.
407 21. Feng X, Yu Y, Zou D, et al. Functional imaging of human retina using integrated multispectral
408 and laser speckle contrast imaging. *Journal of biophotonics* 2022;15:e202100285.
409 22. Huang Z, Jiang Z, Hu Y, et al. Retinal choroidal vessel imaging based on multi-wavelength
410 fundus imaging with the guidance of optical coherence tomography. *Biomedical Optics Express*
411 2020;11:5212.
412 23. Francis JH, Pang CE, Abramson DH, et al. Swept-source optical coherence tomography
413 features of choroidal nevi. *American Journal of Ophthalmology* 2015;159:169-176. e161.
414 24. Alterini T, Díaz-Doutón F, Burgos-Fernández FJ, González L, Mateo C, Vilaseca M. Fast visible
415 and extended near-infrared multispectral fundus camera. *Journal of biomedical optics*
416 2019;24:096007-096007.
417 25. de Carvalho ER, Hoveling RJ, van Noorden CJ, Schlingemann RO, Aalders MC. Functional
418 imaging of the ocular fundus using an 8-band retinal multispectral imaging system. *Instruments*
419 2020;4:12.
420 26. Burgos-Fernández FJ, Alterini T, Díaz-Doutón F, et al. Reflectance evaluation of eye fundus
421 structures with a visible and near-infrared multispectral camera. *Biomedical optics express*
422 2022;13:3504-3519.
423 27. Venkatesh R, Pereira A, Sangai S, et al. Variability in imaging findings in choroidal nevus using
424 multicolor imaging vis-à-vis color fundus photography. *Journal of Current Ophthalmology*
425 2020;32:285.
426 28. Azzolini C, Di Nicola M, Pozzo Giuffrida F, et al. Retromode Scanning Laser Ophthalmoscopy
427 for Choroidal Nevi: A Preliminary Study. *Life* 2023;13:1253.
428 29. Xu Y, Lou L, Wang Y, et al. Epidemiological study of uveal melanoma from US surveillance,
429 epidemiology, and end results program (2010–2015). *Journal of Ophthalmology* 2020;2020.
430 30. Standardization IOF. Ophthalmic Instruments-Fundus Cameras-International Standard, ISO
431 10940. 2007.
432 31. Rahimi M, Rossi A, Son T, et al. Evaluating spatial dependency of the spectral efficiency in
433 trans-palpebral illumination for widefield fundus photography. *Biomedical Optics Express*
434 2023;14:5629-5641.
435 32. Toslak D, Son T, Erol MK, et al. Portable ultra-widefield fundus camera for multispectral
436 imaging of the retina and choroid. *Biomedical optics express* 2020;11:6281.
437 33. Sanchez-Brea LM, Quiroga JA, Garcia-Botella A, Bernabeu E. Histogram-based method for
438 contrast measurement. *Applied optics* 2000;39:4098-4106.
439 34. Ma F, Yuan M, Kozak I. Multispectral Imaging (MSI): Review of Current Applications. *Survey*
440 *of Ophthalmology* 2023.
441 35. Bird AC. Therapeutic targets in age-related macular disease. *The Journal of clinical*
442 *investigation* 2010;120:3033-3041.

443

444 **Figure 1.** A) Optical layout of the system with trans-palpebral illumination, B) Light
445 penetration in the retina and choroid (modified from ³⁵), C) visible and NIR LED spectra.

446 **Figure 2.** A) Representative images of a choroidal nevus, A1) SLO image, A2) enlarged
447 nevus region, B1) Cropped green channel of SLO corresponding to red-dashed circle in the
448 SLO image, B2) red channel of SLO, B3) AF image, B4) NIR reflectance image, C)
449 Multispectral fundus images captured using C1) 625 nm, C2) 780 nm, C3) 850 nm, and C4)
450 970 nm trans-palpebral illumination, D) Enlarged nevus region in the fundus images
451 captured using D1) 625 nm, D2) 780 nm, D3) 850 nm, and D4) 970 nm trans-palpebral
452 illumination, enlarged nevus region in E1) green channel and E2) red channel of SLO, E3)
453 AF, and E4) NIR reflectance images.

454 **Figure 3.** A) The intensity profile of the nevus in the fundus images along the green dashed
455 line in Figure 2 (D1), B) the intensity profile of the nevus in the green and red channels of
456 SLO, AF, and NIR reflectance images.

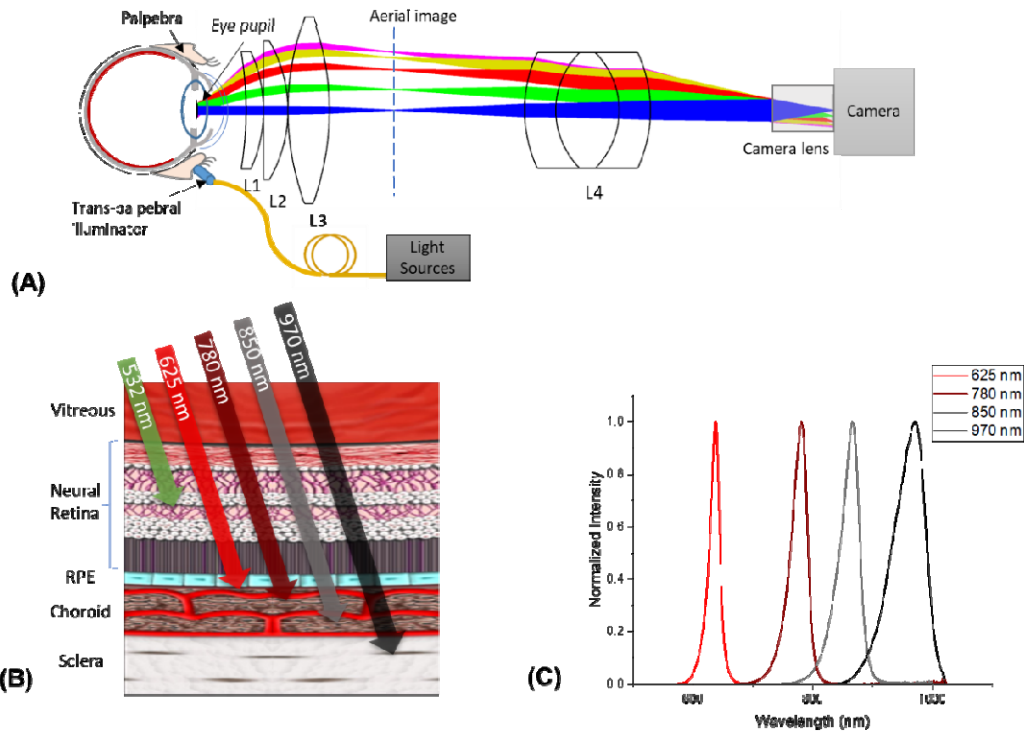
457 **Figure 4.** Analysis of OCT scan of the nevus region A) The B-scan line is shown in the NIR
458 reflectance image, B) corresponding OCT B-Scan, C) the mean intensity en face projection
459 maps of OCT B-scans corresponding to highlighted layers in (D), D) OCT image volume of
460 the nevus region after registration and flattening.

461 **Table 1.** Characteristics of participant subjects and comparative analysis: Nevus basal
 462 diameter measurement in OCT B-Scan vs. widefield fundus images with NIR illumination,
 463 and nevus contrast comparison between multispectral fundus images and the SLO image.

Subject	Eye	Sex	Nevus diameter (μm)				Nevus Contrast (%)				
			OCT scan	Fundus 780 nm	Fundus 850 nm	Fundus 970 nm	SLO-(red)	Fundus 625 nm	Fundus 780 nm	Fundus 850 nm	Fundus 970 nm
1	OD	F	2570	2475	2495	2534	10.88	42.34	73.33	63.05	67.48
2	OD	M	2386	2427	2430	2642	8.79	22.69	66.26	65.37	60.25
3	OD	M	2691	2574	2663	2722	5.59	-	59.10	50.35	54.18
4	OS	M	1847	1950	1881	1861	8.57	56.31	74.81	74.24	59.21
5	OD	F	1607	1591	1560	1549	17.43	60.62	70.10	59.89	55.14
6	OS	F	1994	1893	1799	1560	22.59	42.68	56.29	53.75	36.75
7	OD	M	3054	2826	2774	2722	16.26	37.04	73.40	74.42	60.83
8	OD	F	1329	1256	1202	1116	10.92	52.92	73.93	70.21	63.51

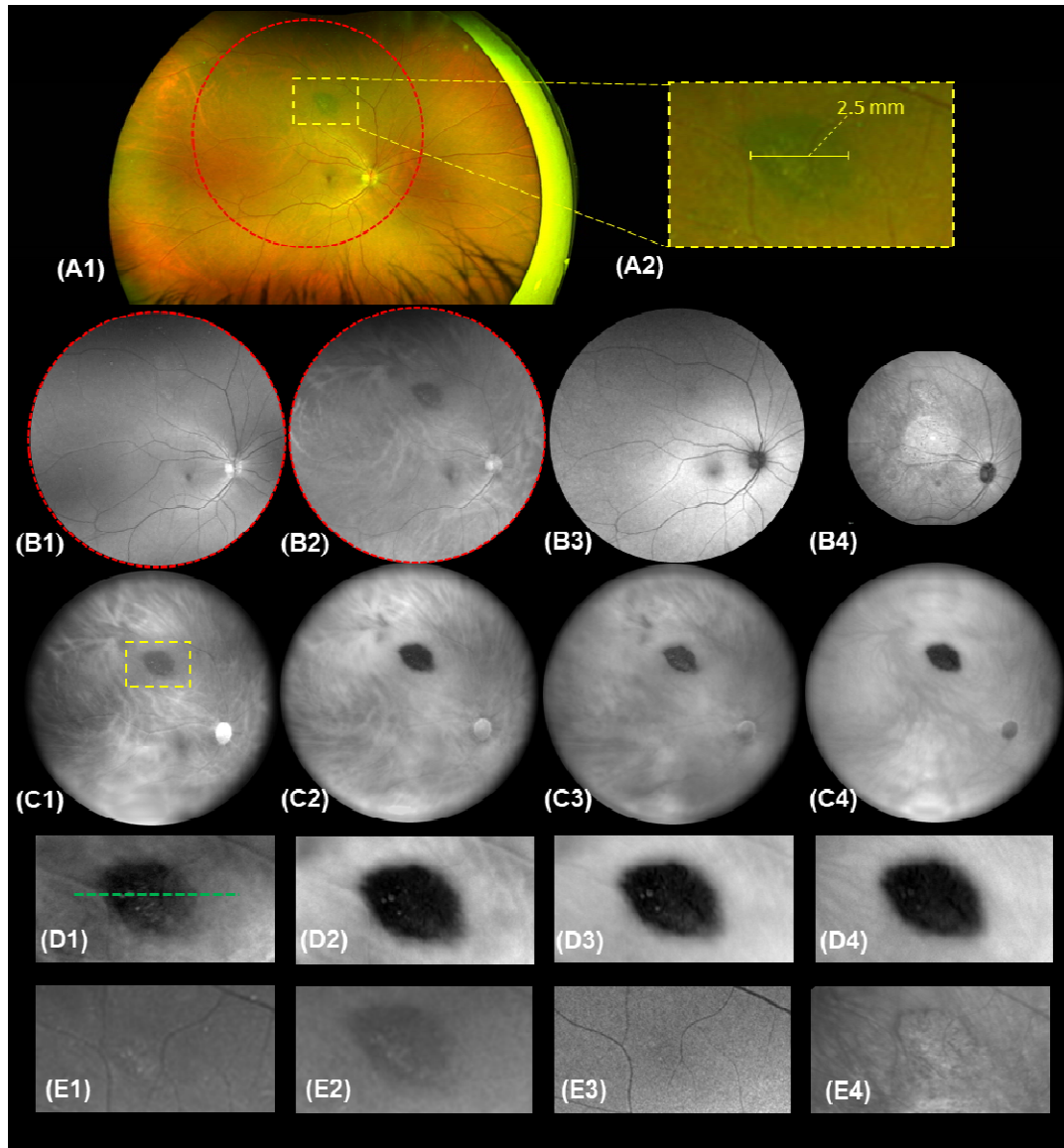
464

465 Figure 1



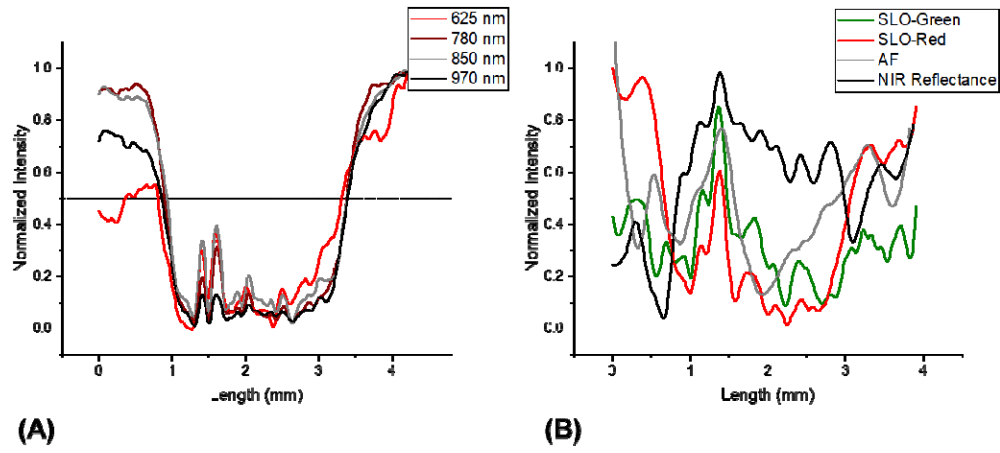
466

467 Figure 2



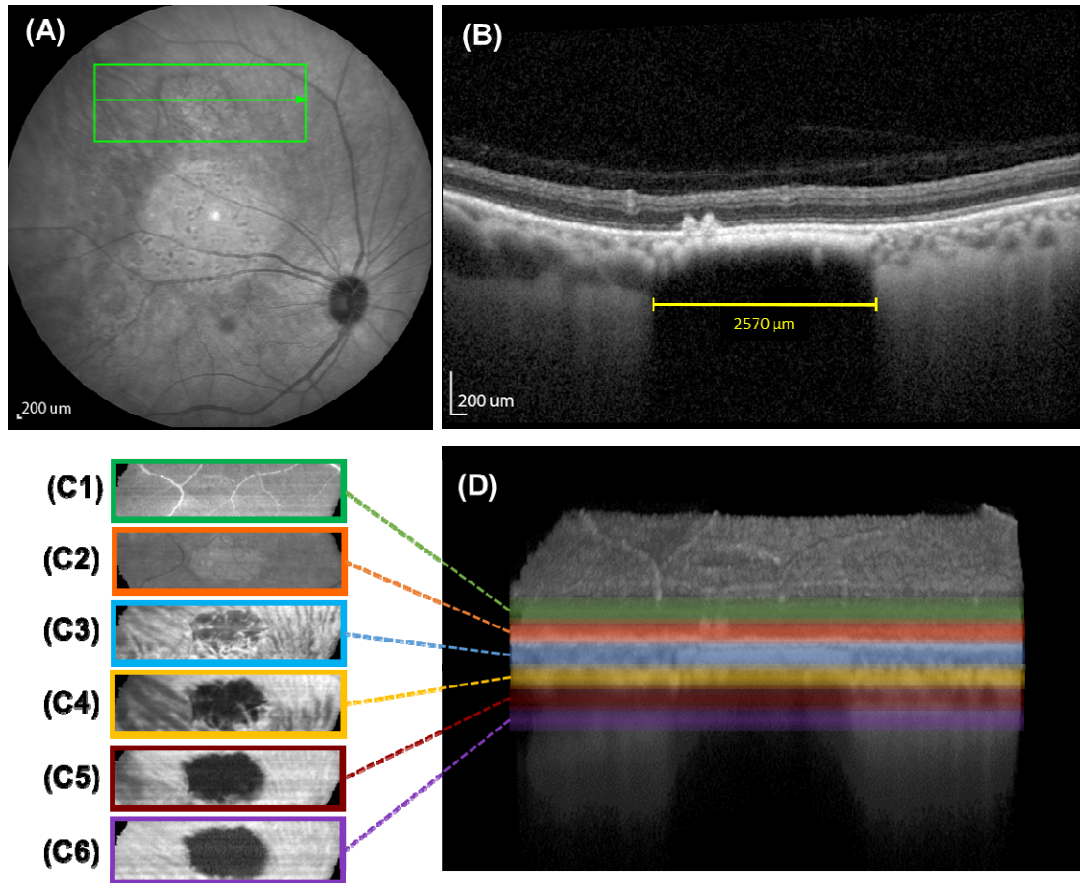
468

469 Figure 3



470

471 Figure 4



472